



1 An Evaluation of the Efficacy of Very High Resolution Air-Quality 2 Modelling over the Athabasca Oil Sands Region, Alberta, Canada

3 Matthew Russell¹, Amir Hakami¹, Paul A. Makar², Ayodeji Akingunola², Junhua Zhang², Michael D. Moran², and
4 Qiong Zheng²

5 ¹Department of Civil and Environmental Engineering, Carleton University, Ottawa, Canada

6 ²Air Quality Research Division, Environment and Climate Change Canada, Toronto, Canada

7

8 Abstract

9 We examine the potential benefits of very high resolution for air-quality forecast simulations using a nested
10 system of the Global Environmental Multiscale – Modelling Air-quality and Chemistry chemical transport model.
11 We focus on simulations at 1km and 2.5km grid-cell spacing for the same time period and domain (the industrial
12 emissions region of the Athabasca Oil Sands). Standard grid-cell to observation station pair analyses show no
13 benefit to the higher resolution simulation (and a degradation of performance for most metrics using this
14 standard form of evaluation). However, when the evaluation methodology is modified, to include a search over
15 equivalent representative regions surrounding the observation locations for the closest fit to the observations, the
16 model simulation with the smaller grid cell size had the better performance. While other sources of model error
17 thus dominate net performance at these two resolutions, obscuring the potential benefits of higher resolution
18 modelling for forecasting purposes, the higher resolution simulation shows promise in terms of better aiding
19 localized chemical analysis of pollutant plumes, through better representation of plume maxima.

20 1 Introduction

21 Numerical modeling of the atmosphere in an Eulerian framework relies on discretization of the computational
22 domain into a numerical grid. The horizontal grid cell size of atmospheric simulations can range in from hundreds
23 of kilometers, to the metre-scale of Large Eddy Simulation models. For the purposes of this study, Very High
24 Resolution (VHR) modelling refers to chemical transport models (CTMs) employing a horizontal grid cell spacing of
25 1km or less. It is in this regime that the photochemical processes may be forecasted with resolved microphysics
26 (e.g. Milbrandt and Yau, 2005(a,b)), and detailed particle and gas-phase chemistry, using currently available
27 computer technology. VHR modelling is very computationally expensive, and also introduces its own set of
28 challenges, such as the availability of surface boundary condition fields as the model grid cell size decreases.
29 Moreover, it is not currently clear whether decreases in model grid cell size leads to more accurate results when
30 compared to observations. The motivation behind VHR modelling in CTMs is to reduce the impact of diluting
31 chemical concentrations - especially from averaging emission plumes into large grid cells – in order to better
32 capture inhomogeneities in emission profiles, to better simulate local transport processes associated with terrain
33 that would otherwise be smoothed by the use of a coarse grid, and to reduce truncation errors and hence achieve



34 better numerical accuracy (Jacobson, 1999).

35 We note here that while the terms “grid cell size” and “resolution” tend to be used interchangeably in the
36 literature, this is not true in a precise mathematical sense; more formally, the ability to resolve features of size
37 $2\Delta x$ requires a grid cell spacing of size Δx , and the highest spatial frequency which can be reconstructed from a
38 discrete sampling of the latter grid cell spacing will be $\frac{1}{2\Delta x}$, the Nyquist wavenumber of the grid cell size
39 discretization. Furthermore, atmospheric models may make use of energy dissipation techniques that broaden
40 the size of resolvable wavelengths to $3\Delta x$ to $4\Delta x$ (Grasso, 2000; Pielke, 2001). Model resolution is thus a function
41 of, but not equivalent to, grid cell size. Here, we define “resolution” as the ability of a model to clearly distinguish
42 components of a predicted atmospheric variable, as a *function* of grid cell size.

43 The issue of a model to distinguish these features is also compounded by uncertainties in model inputs. For
44 example, in a large rural setting, a large model grid cell will represent an area containing many roads, whose
45 emissions will be averaged into one value per species per time. As the grid cell size decreases however, this
46 averaging effect will be reduced, giving each road’s emissions more impact on the resulting concentrations in the
47 grid cell containing it. However, the smaller grid cell size will also result in steeper concentration gradients in the
48 model between adjacent grid cells, which can in turn result in numerical instabilities that contaminate predictions
49 (Salvador, et al., 1999). At the same time, a reduction in grid-cell size can be shown formally to reduce
50 inaccuracies in the discretization of the governing equations for atmospheric motion (Coiffier, 2011). Previous
51 efforts to address these issues through variable grid size or structure in air quality modeling have not received
52 sustained attention, and therefore most current air quality models use a uniform (albeit nested) grid cell size in
53 applications (Garcia-Menendez *et al.*, 2010; Kumar *et al.*, 1997).

54 As resolution increases further, the shape of local topographical features (*e.g.* buildings and street canyons)
55 become more important. Both the increased topographic complexity, and potential numerical instabilities can
56 lead to differences in meteorological forcing as resolution increases (Wolke, *et al.*, 2012; Gego, *et al.*, 2005)). The
57 contribution of meteorological uncertainties due to resolution become more significant, especially for secondary
58 pollutants such as ozone (Valari and Menut, 2008) or secondary Particulate Matter (PM). For example, Markakis
59 *et al.* (2015) in their analysis of 4 km CHIMERE simulations for the relatively flat terrain of Paris, France, suggested
60 that model meteorological grid cell size does not significantly impact forecast accuracy. That may not have been
61 the case, had their terrain been more complex. In contrast, Queen and Zhang (2008) observed considerable
62 meteorological sensitivity to the more complex terrain in their 4 km resolution Community Multiscale Air Quality
63 (CMAQ, EPA 1999) model simulations simulation over the Appalachian Mountains in the eastern United States.

64 A number of studies, employing various approaches, have tried to evaluate the benefits of higher resolution
65 simulations by quantifying sub-grid variability by employing larger model grid cell sizes (Vardoulakis *et al.*, 2003;



66 Ching *et al.*, 2006; Pepe *et al.*, 2016). These studies have often demonstrated that failure to account for higher
67 resolution features may result in mischaracterization of concentrations or health impacts (Isakov *et al.*, 2007).
68 Population exposure studies using air pollution models may be affected by resolution in a more complex fashion,
69 given that both the predicted field (a pollutant with a known health impact) and the data to which the predicted
70 field is to be linked (the human population) both have resolution dependencies.

71 Terrain and meteorology are not the only factors that contribute to greater uncertainties as horizontal grid cell
72 size is reduced – for example, the ability of the model to locally resolve emission fluxes may also become a factor.
73 This may result in improved or deteriorated model performance as the size of the grid cells decrease. Gridded
74 model emissions may have an intrinsic resolution dependence in the underlying spatial disaggregation fields, and
75 this can contribute to uncertainties and errors in emissions as grid cell size is decreased. For instance, Valari and
76 Menut (2008) found that the discrepancy between their modelled and observed concentrations grew, rather than
77 shrank, in response to decreases in grid cell size from 48km to 6 km, and they associated these results with
78 changes in the resulting local emission fluxes. They showed that in their model setup, with regard to ozone, a grid
79 cell size was reached (12x12 km²) where errors in inputs (errors in the emission inventory, wind direction, *etc.*)
80 outweighed the importance of other sources of model error such as grid cell size. The authors however noted that
81 Paris' ozone photochemistry very often resides on the transition between a NO_x⁻ sensitive and a VOC-sensitive
82 regime (Sillman *et al.*, 2003). These are chemical conditions which can alternatively produce or titrate ozone, and
83 hence has a degree of sensitivity to precursor emissions, and therefore, also, to any errors in those emissions.
84 Conversely, in a 3-level nested 9- to 3- to 1- km MM5–CMAQ simulation over Osaka, Japan, Shrestha *et al.*, (2009)
85 found that ozone comparisons to observations improved as the grid resolution increased. This was also the case
86 for a 36- to 12- to 4-km nested MM5–CMAQ simulation over Houston, USA (Ching *et al.*, 2006), where the ozone
87 forecast improvement associated with higher resolution was attributed to the ability of the finer grid cell size
88 model nests to adequately resolve high concentrations of freshly emitted NO_x and hence allow for more local
89 ozone titration. The latter process might not take effect until the grid cell size is sufficiently fine to resolve the NO_x
90 source patterns (*i.e.*, a level where traffic and industrial sources can be identified.) This titration was not seen until
91 they decreased their grid cell sizes to 2 km and smaller. Stroud *et al.* (2011) noted a similar grid cell size
92 dependent chemical impact on model performance, where secondary organic aerosol formation maxima were
93 better simulated with a 2.5km grid cell size model than a 10km grid cell size model. In general, the impact of
94 resolution on model performance appears to depend on a number of factors, such as the terrain, spatial
95 distribution of sources, pollutant of concern, season, *etc.* (Arunachalam *et al.*, 2006; Queen and Zhang, 2008; Dore
96 *et al.*, 2012).

97 Whether or not simulated quantities improve with reference to observed quantities as applications approach VHR
98 grid cell sizes, the resulting *distribution* of the quantities tends to be more physically realistic (Dore *et al.*, 2012;
99 Salvador *et al.*, 1999; Valari and Menut, 2008).



100

101 The benefits for model performance with increased spatial resolution are unclear, based on the above literature.
102 However, most papers converge towards the following qualitative conclusions:

103 1. The impact of terrain topology on meteorological forcing as grid cell size decreases can dwarf the impact of
104 a more accurate spatial apportionment of the corresponding emissions.

105 2. Decreases in grid cell size result in a more realistic spatial distribution of chemical species, whether or not
106 model performance is improved.

107 3. Uncertainties of spatial and temporal emissions allocation have an increasing influence on overall model
108 uncertainty as model grid cell size decreases.

109 The 1980's saw several studies in which the potential impacts of wind direction errors on dispersion model
110 performance were examined. Fox (1981) noted that pairing of model output at observation station locations could
111 be done as a function of both time and space, as a function of time (combining the data across all stations), as a
112 function of space (combining all times, at each station location), or without any pairing (observations and data are
113 compared as cumulative frequency distributions). The accuracy of regulatory dispersion models in the early 1980's
114 was such that Fox (1984) concluded that model and observation values paired in time and space exhibited "little to
115 no correlation" and discussed potential errors associated with transport. Poor correlations were also noted by
116 Hanha (1988), reporting on the first generation of reactive-transport models, stated "wind direction errors are the
117 major cause of the poor agreement in hourly predictions of concentrations at short distances downwind of point
118 sources," as well as describing metrics for air-quality model evaluation. Hanha (1988) also noted that model
119 predictions could be offset in space and time relative to observations, leading to poor performance statistics,
120 despite a greater degree of similarity of behavior if the offsets are taken into account. Errors in wind-field
121 modelling were described as the main source of error in simulations of plumes by Carhart *et al* (1989), again
122 showing how better agreement resulted when model and observations were unpaired in time and/or space, and
123 noted that other metrics such as maximum plume width might better represent model performance. Lee (1987)
124 found that small perturbations in space and time could result in poor correlations, despite similar histogram
125 distributions of both model and observations.

126 More recently, Kang *et al.*, (2007) examined the concept of using the area of the limiting resolution of the model (2
127 to $3\Delta x$, where Δx is the horizontal grid cell size) to weight or spatially average model evaluation metrics for a single
128 grid-cell size, noting how the model's rated ability to capture high concentration events ("hits") was increased when
129 the limiting resolution of the model was incorporated into the performance metrics. However, the use of averaging
130 may mask the potential for a model with a small grid cell size to contain both the desired plume magnitude, as well

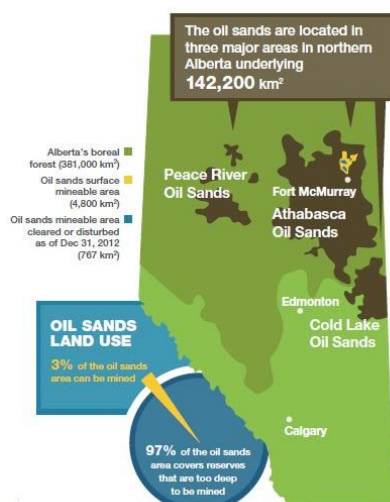


131 as much lower concentrations, within the same larger representative area, masking the potential impact of the
132 reduction in grid cell size.

133 We expand on this concept to evaluate the impact of model grid cell size in the context of an equivalent area about
134 a given observation location. We examine area-weighted metrics in the form of averages over roughly equivalent
135 areas for different model grid cell sizes, and also use the *a priori* knowledge of the observations to determine
136 whether the closest match to observations may be found within an equivalent area. We show that the latter metric
137 demonstrates a positive impact of model grid cell size on simulation results, while more simple paired comparisons,
138 and averages over similar areas, mask these benefits.

139 We examine the impact of grid cell size on model performance in a region of intense petrochemical extraction and
140 upgrading, the Athabasca Oil Sands Region (AOSR). The AOSR refers to the northernmost of three large bitumen
141 deposits located the northern part of the province of Alberta in Canada; the Athabasca, Peace River, and Cold Lake
142 areas. Together these areas cover 142,200 km² in total, and constitute the third largest oil reserves in the world
143 (Government of Alberta, 2016), as shown in Figure 1. The oil sands sector is the second largest source of SO₂ and
144 the third largest source of industrial NO_x in the province of Alberta. This sector is also a significant source of
145 industrial PM, CO, and Volatile Organic Compound (VOC) emissions (Zhang *et al.*, 2018), from a variety of source
146 types and industrial processes (*e.g.* open pit mine tailings ponds, large diesel fleets, bitumen upgrading facilities).
147 As is described below, very high resolution emissions data are available for these sources, and emissions take place
148 in a region with significant topography, hence the region provides a good test case for the relative impact of grid
149 cell size on air-quality model prediction results.

150 We describe next our model, the simulation domains and forecasting setup, the emissions data, our evaluation
151 methodology, and the results of our analysis.





153 Figure 1. Map showing the Oil Sands regions (Government of Alberta, 2016).

154



155 2 Methodology

156 2.1 GEM-MACH

157 The air-quality model used in this work is Environment and Climate Change Canada's (ECCC) Global Environmental
158 Multiscale – Modelling Air-quality and Chemistry (GEM-MACH) model, which has been in use as Canada's
159 operational air-quality forecast model since 2009 (Moran *et al.*, 2010). GEM-MACH is an on-line model, that is,
160 both meteorological and chemistry processes are handled within a single model. The chemical processes reside
161 within the physics module of the Global Environmental Multiscale meteorological forecast model (Côté, *et al.*,
162 1998(a,b)), originate with Environment Canada's earlier off-line model (A Unified Regional Air-quality Modelling
163 System; AURAMS, Gong *et al.*, 2006), and include process representation for particle microphysics (Gong *et al.*,
164 2003(a,b)), inorganic heterogeneous chemistry (Makar *et al.*, 2003), aqueous phase chemistry, in-cloud and below-
165 cloud scavenging (Gong *et al.*, 2006), and secondary organic aerosol formation (Stroud *et al.*, 2011). GEM-MACH
166 employs a sectional approach to represent the size distribution of atmospheric particles, with 12-bin (Makar *et al.*,
167 2015(a,b); Gong *et al.*, 2015) or 2-bin configurations (Moran *et al.*, 2010). The latter configuration is designed for
168 maximum computational efficiency, with re-binning to the 12-bin distribution for key particle microphysics
169 processes, in order to improve accuracy. Here, the 2-bin version of the model has been used, the main focus of the
170 work being the impact of horizontal grid cell size on model results. Eight aerosol chemical components are resolved
171 in GEM-MACH (sulphate, nitrate, ammonium, elemental carbon, primary organic aerosol, secondary organic
172 aerosol, sea-salt and crustal material). In the present study, we make use of GEM-MACH v.1.5.1, described in more
173 detail in Makar *et al.*, 2015(a,b), employing 80 levels in a hybrid vertical coordinate system extending up to 0.1hPa
174 (~30km).

175 2.2 Model Setup

176 2.2.1 Grid Nesting

177 Four levels of nesting have been employed in our simulations, shown in Figure 2(a). This version of GEM-MACH
178 operates on a rotated latitude-longitude coordinate system wherein the position of the coordinate system poles
179 may be set by the user, allowing rotations of the grid with decreasing grid cell size during nesting. The outermost
180 nested grid corresponds to the westernmost $\frac{2}{3}$ of the operational GEM-MACH forecasting domain, with a 10km
181 grid cell size. Within that is nested a 10km grid cell size western Canada domain (yellow region, Figure 2(a)) which
182 has been rotated to match the horizontal orientation of the Rocky Mountains, and which makes use of a similar
183 double-moment microphysics scheme (Milbrandt and Yau, 2005 (a,b)) as the two innermost domains – this
184 intermediate nested grid was constructed in order to allow hydrometeors to be passed from the western Canada
185 10km domain to the two innermost domains with a minimum of spin-up time required for the inner domain's
186 meteorology. The third nested grid inwards (green region, Figure 2(a)) is the 2.5km grid cell size domain, which
187 covers most of the Canadian provinces of Alberta and Saskatchewan. This grid will hereafter be referred to as the
188 OS2.5km domain. The fourth and final nested grid (blue square, Figure 2(a)) is a 1km grid cell size domain, roughly
189 centered over and covering the immediate environs of the Athabasca Oil Sands, and is referred to hereafter as the
190

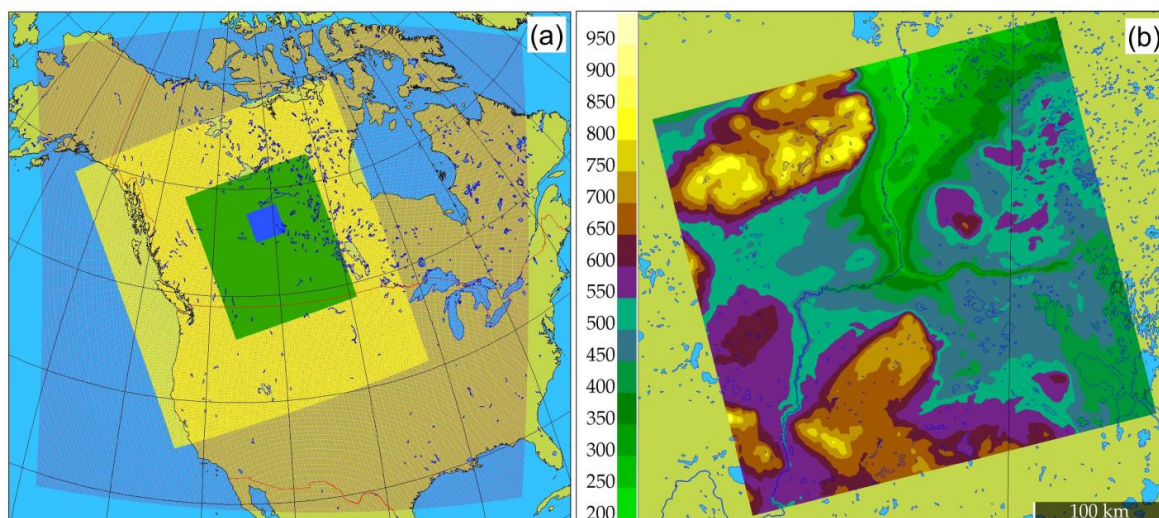


191 OS1km model. This last nest also shows the region within which 22 instrumented aircraft flights were conducted
192 during August and September of 2013, providing a unique measurement dataset for our evaluation of the
193 OS2.5km and OS1km model output for the same time period. Table 1 provides details on the horizontal
194 dimensions of each of these nested domains, and the duration of the simulations on each grid. All four model
195 nests make use of the same vertical coordinate and levels. Figure 2(b) shows the topography of the 1km domain
196 in detail; the region to be modelled is situated in a broad river valley, with a local vertical relief of 750 m.
197 Significant wind shears and frequent inversions are observed in the region, and part of our interest in 1km grid cell
198 size simulations is to determine the extent to which these local features may influence model prediction accuracy.

199 2.2.2 Simulation Cycling Strategy

200 The forecasts run in a repeating cycle from new meteorological analyses on every 36 hours, and hence are
201 constrained by observations to present chaotic drift of the forecast over an extended simulation. The outermost
202 10km domain carries out a 36 hour forecast, of which the first 6 hours is discarded as spin-up; the final 30 hours is
203 used as initial and boundary conditions for the rotated 10 km grid cell size domain (the OS10km domain). As
204 noted above, the OS10km domain makes use of a microphysics package matching that of the subsequent higher
205 resolution simulations for better matching of cloud fields at those resolutions. An OS10km simulation of 30 hours
206 is then carried out, with the first 6 hours being discarded as spin-up, and the latter 24 hours forming the initial and
207 boundary conditions for the 2.5 km grid cell size OS2.5km simulation. The OS2.5km simulation is of 24 hours
208 duration. The OS1km simulation covers the same 24 hours (and hence both 2.5km and 1km simulations start from
209 the same OS10km initial conditions at for every 24 hour forecast), with the 2.5km simulation providing boundary
210 conditions thereafter to the OS1km model. Continuity between 24 hour forecasts is thus maintained at the level of
211 the outermost nest. The outermost domain is cycled every 12 hours starting at 0UT and 12UT; however, we have
212 selected the set of contiguous OS2.5km and OS1km 24 hour simulations starting from the 12UT continental
213 domain for our comparison.

214 Meteorological boundary conditions for lowest resolution GEM-MACH simulations are taken from operational
215 GEM forecasts, in turn driven by data assimilation analyses performed at the Canadian Meteorological Centre.



216
 217 Figure 2. (a) The four nested domains of the GEM-MACH simulations. From outermost to innermost domains,
 218 these are CONT10km (outermost, red dots), OS10km (yellow), OS2.5km (green), and OS1km (blue). The model
 219 simulations from the two innermost domains are the focus of the present study. (b) Topography in the OS1km
 220 domain centred on Fort McMurray, Alberta (m agl). The coloured area corresponds to the central blue domain in
 221 (a).

222 Table 1. Nested Domain Specifications

Parameter	CONT10km	OS10km	OS2.5km	OS1km
Grid Size	520x520	318x280	643x544	318x324
Time step size (s)	300	300	60	20
Hours simulated	36	30	24*	24*

223 *Note that both OS2.5km and OS1km output frequency was hourly.

224 2.3 Model Emissions

225 All emissions data used in this work are described in Zhang *et al.* (2018). These emissions data include (a) direct
 226 observations of stack-specific hourly emissions measured by Continuous Emission Monitoring Systems (CEMS), (b)
 227 regional emissions inventory data from the Cumulative Environmental Management Association (CEMA) - which
 228 had the most detailed stack and process level emission data for the AOSR facilities, including emissions from mine
 229 faces, tailings ponds, and the off-road mining fleet), (c) the 2010 Canadian Air Pollutant Emissions Inventory (APEI)
 230 - which is the most comprehensive national emissions inventory, and which has the largest spatial coverage for



231 area sources for areas outside the AOSR, and (d) the 2013 National Pollutant Release Inventory (NPRI) (a subset of
232 the APEI) that is based on emissions reports from large industrial facilities.

233 These emissions data sets primarily describe emissions of pollutants known as criteria-air-contaminants (NO_x,
234 VOCs, SO₂, NH₃, CO, PM_{2.5}, and PM₁₀) for *major-point sources* (i.e., large emission stacks) and *area sources*. Area
235 emissions sources typically consist of multiple small mobile sources spread over a large area (e.g., off-road
236 vehicles), large flux sources such as mine tailings settling ponds or mine faces, and/or large numbers of small
237 stacks for which no stack characteristic data (volume flow rates, temperatures of emissions, stack diameters),
238 needed to estimate plume-rise heights, are available.

239 Major-point sources are represented by a single geographical (latitude, longitude) pair of coordinates, and are
240 assigned to the grid cell in which the point is located. These sources are likely to be the most impacted by model
241 horizontal grid cell size, as even a large major-point source plume, which in reality may only occupy an emissions
242 area on the order of 100 m², is represented by a flux spread over an entire grid cell. A plume from a major point
243 source within a 2.5km grid cell will thus be immediately diluted to a size of 6.25km² upon emission, whereas the
244 same source with a 1km grid cell will have a cross-sectional horizontal extent of 1km². At the same time, higher
245 resolution may require a much more accurate representation of model winds close to the sources to maintain
246 accuracy in evaluation metrics dependant on plume position such as correlation – a wider plume being more likely
247 to at least partially intersect a monitoring station location than a narrower plume.

248 Area sources that are large compared to both model grid cell sizes (2.5km and 1km) can be expected to be
249 approximated by model grid cells of both resolutions, and are thus expected to be less impacted by model
250 resolution than emissions from point sources. However, smaller area sources (i.e. areas intermediate between
251 2.5km and 1km to the side) may be better resolved, and hence have less dilution and higher downwind
252 concentrations, when higher spatial resolution is employed.

253 In the AOSR, approximately 95% of the SO₂ emissions originate in major-point sources, while NO₂ is
254 apportioned ~40% to major-point sources and ~60% to area sources (Zhang *et al.*, 2018). Consequently our *a*
255 *priori* expectation is that the impact of the resolution change will be strongest for species like SO₂, less strong for
256 species like NO₂ that are emitted in part by point sources, but may also be apparent for other species and
257 secondary products, such as O₃.

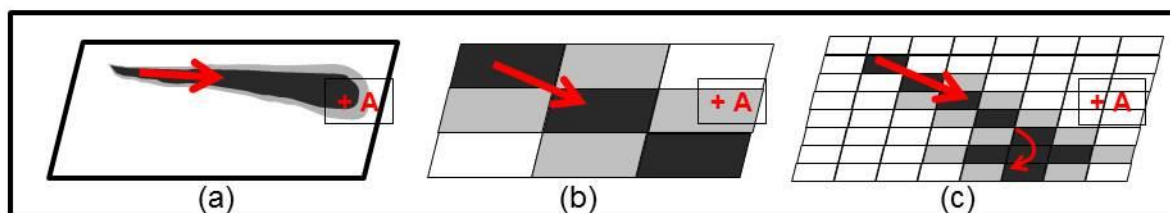
258 2.4 Model Evaluation Methodology and Metrics

259 Comparisons between air-quality models and observations usually take the approach of comparing observation
260 and model-generated values paired in time and space, from the observation location and corresponding model
261 grid-cell respectively. We refer to this approach hereafter as our “standard” evaluation, for both 2.5km and 1km
262 simulations. However, we note additional factors aside from grid-cell size may influence the outcome of air-



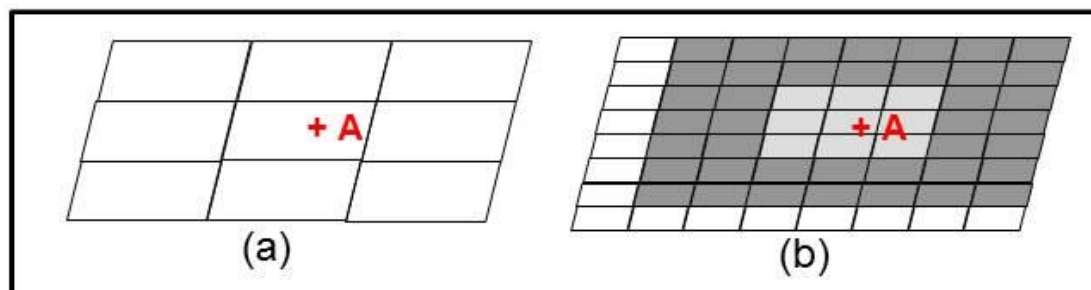
263 quality model evaluations. For example, the relative skill of the meteorological component of the air-quality
264 model will depend in part on the density of meteorological observation data, incorporated into the model via data
265 assimilation, for the construction of the model's initial meteorological state. This in turn will influence the local
266 skill of the model's predicted wind directions and hence the skill of its plume transport. The simulations carried
267 out here focus on the Fort McMurray area, where the nearest available upper air meteorological sounding site is
268 located at the ECCC Stony Plain station, located approximately 500km south-west of the study area. The
269 advantage of higher resolution simulations (*e.g.*, reduced numerical error associated with the discretization of
270 transport operators, and better treatment of local topographic influences) may thus be offset by errors in the
271 predicted *large scale* flow.

272 While meteorological model synoptic-scale forecast errors may manifest themselves locally as errors in the
273 direction of winds driving local plume transport, other advantages may result from the use of higher resolution
274 air-quality models. Since lower resolution models *de facto* instantaneously redistribute plumes emitted from
275 large stack sources over a larger area, such artificial diffusion will reduce the model's ability to accurately simulate
276 concentration maxima, and the resulting chemistry, within simulated model plumes. However, the spatial extent
277 of a plume in a model employing a large horizontal grid cell size may be such that its existence may be captured at
278 discrete observing sites. In contrast, forecast plumes in models with smaller horizontal grid cell sizes may
279 correctly capture plume magnitude and chemical behaviour, but may be more subject to errors in the larger scale
280 wind direction. To illustrate this point, Figure 3 shows a conceptual diagram of an actual plume, a large grid cell
281 size model plume, and a small grid cell size model plume, where the latter two simulated plumes are both subject
282 to the same synoptic-scale error in wind forecast direction (indicated by large red arrows; the smaller red arrow in
283 Figure 3(c) indicates the impact of local forcing predicted for the second model). Observation station "+A" is
284 located downwind, and records the presence of the actual plume (Figure 3(a)). The coarse grid cell size simulated
285 plume (Figure 3(b)), despite the error in the forecast wind direction, captures part of the observed plume in the
286 resulting time series at the observation station location. In contrast, the small grid cell size plume (Figure 3(c)),
287 despite resolving the plume shape (and plume-internal chemistry) to a greater degree than the coarse grid cell size
288 simulated plume, fails to record the presence of the plume at the observation location. A simple paired
289 observation-model time series evaluation would thus suggest that the former model has superior performance to
290 the latter model in this example, despite the latter model having created a more "realistic" plume in terms of the
291 maximum concentration reached, albeit in the wrong location, due to synoptic-scale forecast wind direction error.
292 In this particular instance, the magnitude of the smaller grid cell size simulated plume is more realistic than that of
293 the coarse grid cell size plume, but this improvement will not be captured in a standard evaluation analysis. Shifts
294 in plume location across individual grid cells away from the location of an *in-situ* observation are more likely grid
295 cell size decreases. In this example, a standard analysis would impose a more stringent expectation on the smaller
296 grid cell size simulation to correctly identify plume locations.



297
298 Figure 3. Schematic comparison of surface concentration contours and model grid cell values of a transported pollutant
299 plume from a large stack (termed a "point" source). Wind direction shown by red arrows. Monitoring station location
300 marked by "+A". (a) Actual plume. (b) Coarse grid cell size air-quality model prediction. (c) Fine grid cell size air-quality model
301 prediction. Note the change in wind direction between observations (a) and simulations (b,c) associated with errors in the
302 forecast of the synoptic wind.

303 In order to attempt to evaluate the potential for higher resolution simulations to provide potential benefits that
304 are masked by synoptic scale forcing errors, in addition to the standard analysis, we perform additional analyses
305 that examine the model's ability to resolve plumes in the *vicinity* of the observation station. This is illustrated in
306 Figure 4.



307
308 Figure 4. Scale diagram of the same region in (a) 2.5km grid cell size simulation and (b) a 1km grid cell size simulation.
309 Region enclosed by light grey / dark grey shading in (b) represents the nearest nine / forty-nine 1km gridpoints surrounding
310 the observation location "A".

311 Figure 4(a) shows an observation station enclosing the nine nearest-neighbour model grid-cells for a 2.5km grid
312 cell size, while Figure 4(b) shows the corresponding 1 km grid cell size map, with the nine nearest-neighbour
313 model grid-cells shown in light grey, the forty-nine nearest grid cells shown in the region enclosed in dark grey.
314 Figure 4(a) encloses a region of 56.25 km^2 ($7.5 \times 7.5 \text{ km}$), while the light grey region in Figure 4(b) encloses 9 km^2 ,
315 and the darker grey region encloses 49 km^2 .

316 As noted above, in a formal mathematical sense, the smallest region resolvable by an Eulerian grid model is twice
317 the size of the model grid cell size (relating to the Nyquist frequency of the model); hence the smallest resolvable
318 feature spans two model grid cells in each direction. However, in a practical sense, a total of nine grid cells
319 centred on the observation station must be used to allow a boundary of two grid cells in any direction. Sampling



320 any or all of the 9 grid cells in Figure 4(a) may thus be said to be representative of the model's ability to simulate
321 events occurring at discrete location "+A". The closest corresponding sampling region available to the 1 km model
322 (Figure 4(b)) is shown in dark grey. The light grey region of Figure 4(b) represents the closest 1 km grid cell size
323 region that corresponds to the single 2.5 km grid cell in which the observation station is located in Figure 4(a). We
324 attempt to ascertain model performance in these approximately equivalent regions around each observation
325 station, in the analysis that follows.

326 Our approach follows two steps:

327 (1) From the 2.5km simulation, in addition to the predicted model value at the grid-cell containing the
328 observation location, we determine the model grid-cell value in the nine grid-cells surrounding the
329 observation station location which has the closest value to that observed at the station. This represents the
330 model's "best estimate" of the value at the observation station location itself, to the model's ability to resolve
331 features at 2.5km grid cell size.

332 (2) From the 1km simulation, in addition to the model value at the grid-cell location, we select the closest value to
333 the observation value from: (a) the nearest nine grid-cells to the observation station location, and (b) the
334 nearest 49 grid-cells to the observation station location. The former represents the model's "best estimate"
335 of the value at the observation station location itself, while the latter represents the 1km model's best
336 estimate in the closest equivalent region to the limiting resolution of the 2.5km model.

337 Comparing the resulting statistical measures of each of these selected values with observations, in addition to the
338 standard analysis, thus evaluates the model's best attempt to resolve features for the specified grid cell size, and
339 allows cross-comparison of model performance within nearly equivalent areas. Cross-comparing the statistical
340 values for the different regions described above shows the model's ability to resolve features such as plumes from
341 the standpoint of the region represented at the different grid cell sizes. If synoptic-scale transport direction errors
342 creates situations similar to that depicted in Figure 3(a), a standard comparison of error would be expected to
343 show little benefit to higher resolution. However, the "best model estimate" comparisons would capture the
344 ability of the higher resolution model to more accurately simulate the magnitude of the plume, if not its spatial
345 location. Each of these selection procedures will be employed in the surface concentration comparisons which
346 follow.

347 We evaluate our model simulations against observations made at surface monitoring networks in the vicinity of
348 the Athabasca oil sands, and aboard an instrumented aircraft, the National Research Council of Canada Convair.
349 For the surface monitoring data, hourly time series of model output were matched to station time series using the
350 different strategies described above. For the aircraft observations, we extract model values through temporal and
351 spatial interpolation to the aircraft's position during the flights and only perform the standard analysis, as well as



352 examining the behaviour of the two simulations along cross-sections corresponding to the flight paths.

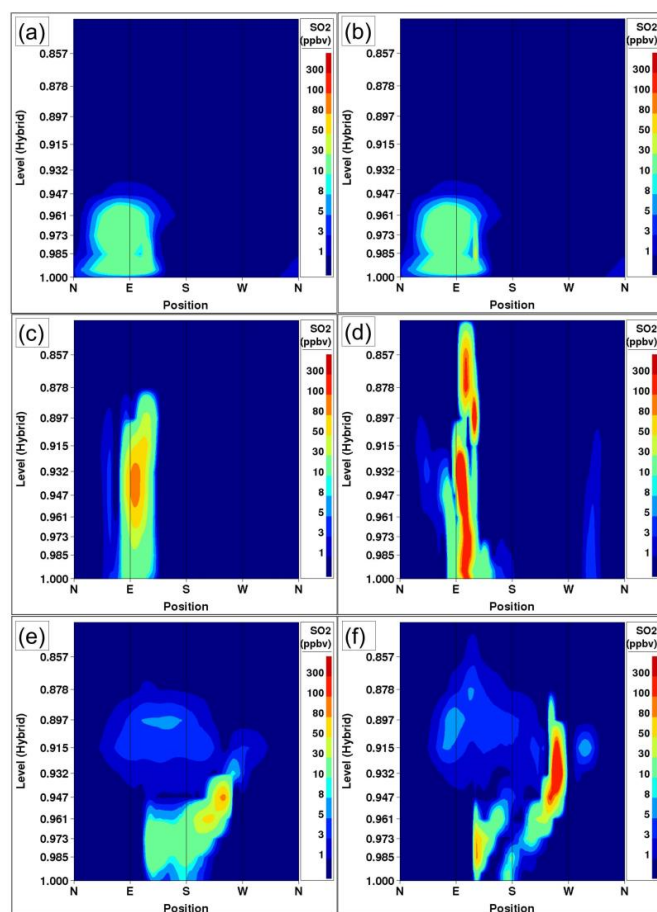
353 Our statistical metrics for evaluation are common to many other air-quality applications, and were computed
354 using the ‘modstat’ function from the OpenAir R package (Carslaw and Ropkins, 2012). The statistics calculated
355 here include: mean bias (MB; perfect score: zero), mean absolute gross error (MGE; perfect score: zero),
356 normalised mean bias (NMB; perfect score: zero), normalised mean gross error (NMGE: perfect score: zero), root
357 mean squared error (RMSE; perfect score: zero), correlation coefficient (r , perfect score: unity), coefficient of
358 efficiency (COE: a perfect score is unity, a zero/negative score means the model is equivalent/less predictive
359 than the mean of the observations), and the index of agreement (IoA; perfect agreement is unity, and -1
360 indicates no agreement or little variability).

361 3 Simulation Comparisons and Evaluation

362

363 3.1 Model-to-model comparisons and averages

364 We begin a comparison of 2.5km and 1km grid cell size for specific events, and for averages across the 1km
365 domain, in order to provide a qualitative comparison of the differences in simulations for the two simulations, and
366 then continue with the quantitative comparison. Figure 5 compares OS2.5km (left column) and OS1km (right
367 column) simulation results for a cross-section located 0.2km from a major SO₂ emissions source at 0, 12 and 24
368 hours into a given simulation day.



369

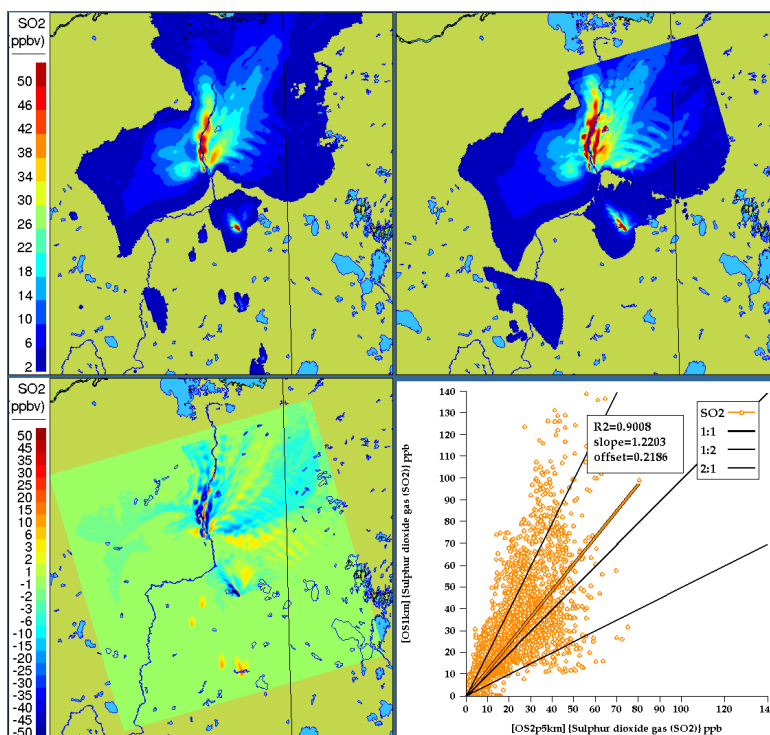
370 Figure 5. Comparison of simulated SO₂ plume mixing ratios (ppbv) located 0.2km from a major point source, for OS2.5km
371 simulations (left column) and OS1km simulations (right column), at 0 (a,b), 12 (c,d), and 24 (e,f) hours into a 24 hour
372 simulation.

373 The model results are identical at hour 0 due to both the OS2.5km and OS1km models being initialized from the
374 OS10km data at this time (small differences in Figure5(a,b) are due to slight mis-matches in the cross-section
375 locations). Subsequent cross-sections show the OS1km model is capable of resolving both higher absolute mixing
376 ratio values, and sharper gradients, within 12 hours of simulation time (Figure 5 (c,d)). Multiple plumes are
377 resolved by 12 hours of simulation time in the 1km grid cell size simulation, along with markedly different plume
378 heights, plume structure, and a factor of two increase in the magnitude of plume mixing ratios relative to the
379 lower grid cell size simulation, and these differences persist into the 24th simulation hour (Figure 5(e,f)). Mixing
380 ratio differences of these magnitudes are to be expected given the increase in resolution, but Figure 5 shows that
381 other important aspects of the predicted plumes have changed. The plume heights are a function of predicted
382 local stability conditions in the grid-square containing the source, and the variation shown here represents a
383 substantial change in the predicted local stability for the origin sources of these plumes, resulting from the change



384 in model horizontal grid cell size.

385 Figure 6 compares the maximum surface SO₂ during the entire period for each simulation, as well as the difference
386 in maximum SO₂ between the simulations, along with a scatterplot of OS2.5km versus OS1km simulation results
387 (where, in the latter two panels, OS2.5km values were assigned to the corresponding OS1km grid-cell locations
388 using the nearest-neighbour approach).



389
390 Figure 6. Comparison of total-simulation *maximum* surface SO₂ mixing ratios (ppbv) at (a) 2.5km and (b) 1km grid cell size
391 (ppbv). (c) Difference (2.5km – 1km). (d) Scatterplot of 2.5km (x-axis) versus 1km (y-axis) total simulation average grid-cell
392 surface SO₂ mixing ratios.

393 The maximum surface concentrations tend to show more elongated structures at the smaller grid cell size;
394 compare Figures 6(a,b), particularly for plumes in the western (left) half of the OS1km domain. The difference
395 plot (Figure 6(c)) shows that local maximum concentration differences of up to -45 ppbv occur, due to changes in
396 the placement and maximum concentration of high concentration plumes. The scatterplot of Figure 6(d) shows
397 that OS1km model has a demonstrated ability to achieve higher concentrations than the OS2.5km model, with a
398 slope of 1.22, and a noticeable clustering of values along the 1:2 line. While these results are not unexpected
399 since approximately 95% of the SO₂ emissions in the domain originate in large stack, or point, sources, and hence
400 initial concentrations at source would be expected to be 6.25x higher in the OS1km simulation, they also suggest that
401 a substantial improvement in the OS1km model's ability to capture SO₂ concentrations *should* be possible. That is,



402 the results of the two models are substantially different, and given the reduction in numerical error expected with
403 employing a smaller grid cell size, the latter might be expected to outperform a larger grid cell size model.
404 However, as we shall demonstrate in the next section, plume placement errors such as depicted in Figure 3 play a
405 substantial role in model performance as grid cell size decreases.

406 3.2 Quantitative comparisons

407

408 3.2.1 Surface observation comparison

409 The locations of the local network of 10 surface monitoring stations located near the sources of emissions in the
410 region (oil sands facilities) are shown in Figure 7. As noted in section 2.4, we carry out several analyses:

411 (1) The standard evaluation (model values are extracted from the model grid-cells containing the observation
412 stations, at both grid cell sizes).

413 (2) Equal areas of representativeness, 1km and 2.5km grid cell sizes (the nearest nine OS1km grid cells are
414 compared to the OS2.5km single cell evaluation in two ways):

415 a. Averaging of the OS1km results across the nine grid cells prior to evaluation (to determine whether
416 the mean value is better represented by the smaller grid cell size, similar to the approach taken in
417 Kang *et al.* (2007)).

418 b. Selection of the *best* of the nine grid cells (closest to the observation value), to determine the extent
419 to which the OS1km model is capable of better representing the concentrations somewhere within
420 the corresponding OS2.5km model grid cell, if not at the OS1km cell closest to the observation
421 location. Higher scores for the 1km grid cell size simulation in this case would indicate that while
422 errors in plume positioning (for example due to errors in the synoptic scale flow) negate some of the
423 advantages of the OS1km simulation, the plume may be better represented by the OS1km simulation
424 within the 2.5km grid cell's area.

425 (3) Equal areas of representativeness and equal regions of variability (nearest nine 2.5km cells are compared to
426 the nearest forty-nine 1km cells). Here we make the assumption that the 2.5km grid cell size model's ability
427 to resolve features is limited to the surrounding three grid cells in each horizontal dimension, and make use of
428 the closest-in-size block of corresponding 1km cells (a 7×7 grid centered on the cell containing the
429 observation point.) In both cases, the model value closest to the observations is chosen prior to evaluation.

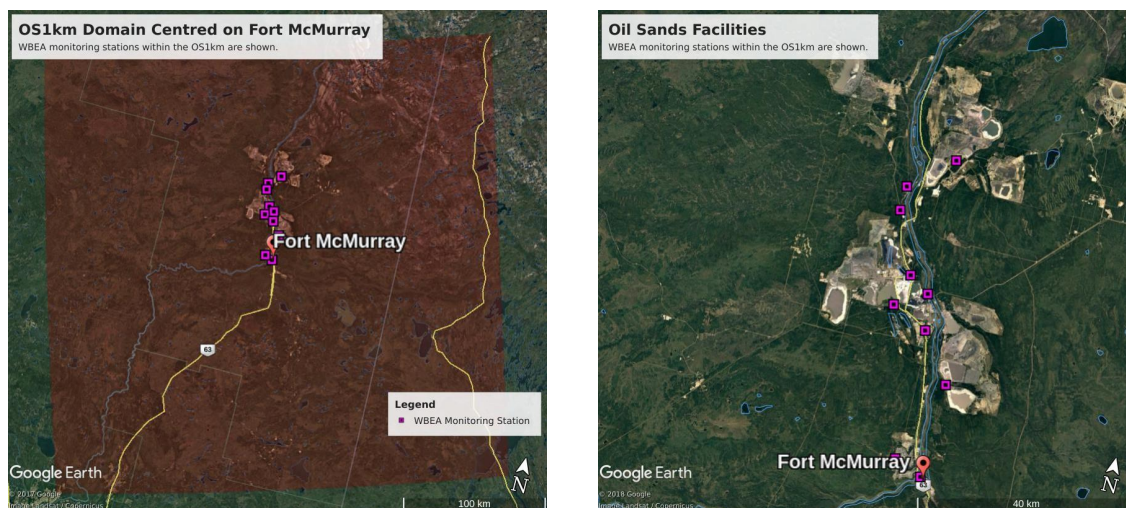
430 While evaluations (2b) and (3) deliberately select the "best" value, they also provide a quantitative estimate of
431 the extent to which each model is capable of achieving the correct answer within roughly equal representative
432 areas centered on the observation station locations. These comparisons are intended to evaluate (a) the
433 extent to which the 1km grid cell size is capable of improving simulation results despite, *e.g.*, the larger scale



434 flow resulting in errors in the plume placement, and (b) whether the 1km grid cell size model is capable of
435 outperforming the 2.5km grid cell size model *over equivalent regions*. In the last test, we place both models on
436 an equal footing with regards to the region being represented, as well with regards to allowing cell-to-cell
437 variability and the selection of a closest match to observations.

438 Our evaluation is presented as tables of statistical metrics. The comparisons employing the nearest neighbour
439 approach are described with a “B#” superscript suffix, denoting that the “Best” sample within a square centred
440 on the observation point containing a total of # grid cells (e.g. the OS1km⁸⁹ label denotes a comparison
441 between observed data and the simulation grid cell within a 3 × 3 grid-cell square centered about the
442 observation point). Similarly, an A# superscript describes a comparison between the observations and the
443 Average of the # square of grid cells centered on the observation point.

444 Comparisons to surface concentrations were performed using publicly available data collected by the Wood
445 Buffalo Environmental Association (WBEA), which operates the air-quality monitoring network residing within
446 the OS1km domain. The monitoring station locations are shown in Figure 7. The statistical performance of the
447 models, calculated using the procedure outlined above, are given in Tables 2 through 5, for SO₂, NO_x, O₃, and
448 PM_{2.5}, respectively.



449
450 Figure 7. Illustration of the OS1km domain, with observation station locations. (a) Entire domain. (b) Close-up
451 view of station locations. Monitoring stations are shown as purple outline squares in both images. Light grey
452 regions in the background satellite image (b) are oil sands open-pit mining operations.

453 In the *standard* model grid cell to observation measurement comparison for SO₂, and NO_x (first two columns,
454 Tables 2 and 3), the OS1km simulation had *worse* scores for all the metrics considered here. For O₃, the OS1km
455 model had the better score for the correlation coefficient and root mean square error, and worse scores for all



456 remaining model evaluation metrics. For $PM_{2.5}$, the OS1km model had higher performance for the correlation
457 coefficient and biases, while the OS2.5km model outperforms the OS1km model for all other metrics examined
458 here. Based on a standard analysis, the OS1km model thus performs poorly compared to the OS2.5km model; the
459 expected advantages associated with reduced numerical error in transport at smaller grid cell sizes are being offset
460 by other factors controlling the net model error.

461 When standard evaluation is compared to the *average* of the nearest nine 1km simulation grid cells surrounding
462 the observation point (first three columns of the tables), an intermediate result appears. For SO_2 (Table 2) the nine-
463 cell OS1km average has the best performance for correlation coefficient - indicating a better time distribution of
464 events may be achieved by a nine cell average at 1km grid cell size. The other metrics for the A9 simulation are
465 intermediate between the two standard evaluations for each simulation, indicating that some of the performance
466 loss resulting from the use of 1km grid cell size is reduced through averaging results to approximately the same size
467 regions as the OS2.5km grid cell size. The latter result holds for all metrics for NO_x (including R, see Table 3). For
468 ozone (Table 4), averaging the nine nearest OS1km grid cells prior to measurement gives the best performance for
469 R and RMSE, and worse performance for the other metrics. For $PM_{2.5}$ (Table 5), all metrics for the OS1km nine grid-
470 cell average aside from the bias fall mid-way between the two standard methodology evaluations. Averaging the
471 smaller grid cell size model results thus shows a marginal improvement, depending on the species, but overall does
472 not compensate for the decrease in performance resulting from going to the smaller grid cell size.

473 We next ask the question, “Does a more accurate simulation value *exist* within the same region of the 1km model
474 as is encompassed by a 2.5km grid cell?” (fourth column of these Tables), by selecting the model value in the
475 nearest nine 1km grid cells with the closest match to observations and comparing to the corresponding single 2.5
476 grid cell. A dramatic improvement in the relative OS1km performance metric scores can be seen. For each of
477 Tables 2 through 5, this “best of nine” 1km comparison outperforms the previous 3 comparisons (columns 1
478 through 3), for all metrics. These improvements are sometimes dramatic (*e.g.* a doubling of correlation coefficient
479 along with a reduction in mean bias by a factor of three, a reduction of NO_x mean bias values by a factor of 3, a shift
480 of coefficient of error from negative to positive values for O_3 , and a reduction in the coefficient of error for $PM_{2.5}$ by
481 a factor of 2.5 compared to the nearest competing value from the previous evaluations. The coefficient of
482 efficiency for SO_2 and O_3 make the transition from negative to positive values when the “best-of-nine” methodology
483 is used, indicating that the model is able to better predict the observations than the observed mean, somewhere
484 within an equivalent area. This evaluation suggests that the OS1km model does *contain* a better result within the
485 same approximate region encompassed by a 2.5km grid cell. However, the location of that better result may be
486 subject to positioning error, such as described in Figure 3.

487 A valid argument could be made that the methodology employed in this fourth evaluation is subject to selection
488 bias, in that the selection of a *best* value in the case of the nearest nine 1km simulation places that model



489 simulation at an advantage relative to the 2.5km model. To address this last issue, the final two additional
490 methodologies for evaluation were employed, still maintaining the same approximate area of representativeness
491 for a grid cell, namely choosing the best value out of the nearest *nine* 2.5km grid cells (the limiting resolution of this
492 model simulation), and the best value out of the nearest *forty-nine* 1km grid cells (fifth and sixth columns of Tables
493 2 through 5, respectively). That is, we attempt to place the two models on an equal basis with regards to selection
494 bias within a given region containing an observation station.

495 Two important results can be seen from this final evaluation. First, as was the case for the “Best of 9” for the
496 OS1km simulation compared to the standard OS1km evaluation, the “Best of 9” for the OS2.5km simulation has a
497 considerably better performance than the standard OS2.5km evaluation (compare fifth and first columns, Tables 2
498 through 5). That is, the OS2.5km model may *also* be subject to location errors in transported species representation
499 which influence model performance. However, when performance within the 56.25 km² area surrounding each
500 measurement point in the OS2.5km “Best of 9” evaluation is compared to the 49 km² area surrounding the
501 measurement points in the OS1km “Best of 49” simulation (*i.e.* compare columns five and six in Tables 2 through 5),
502 it can be seen that the OS1km model outperforms the OS2.5km model for all metrics for O₃, and PM_{2.5}, and all
503 metrics aside from bias for SO₂ and NO_x. That is, despite the OS1km model having a slight disadvantage in the
504 relative size of the representative area containing the measurement station location, and both models being
505 allowed a similar selection strategy, the OS1km model is capable of generating values closer to the observations
506 than the OS2.5km model within an equivalent sub-region, across most of the metrics and chemical species
507 considered here.

508 This final result is strongly suggestive of the presence of issues such as illustrated in Figure 3. These may include
509 errors in the larger scale synoptic wind flow, combined with the reduced size of plumes as grid cell size is reduced,
510 leading to more “misses” than “hits” for a given recorded event at a measurement station compared to the coarse
511 grid cell size model. There may be multiple additional causes for such errors (examples include poor observation
512 density in the region for model initialization, underlying lower resolution boundary condition fields such as
513 topography not improving with the reduction in grid cell size, inaccuracies in land use fields used in meteorological
514 modelling due to rapid development, and errors in other aspects of the reaction transport modelling system aside
515 from horizontal resolution). The expected advantages of the small grid cell size, such as better representation of
516 the concentrations of species within plumes and hence better representation of their reactive chemistry (c.f.
517 Lonsdale *et al.*, 2012), may be lost in a standard performance analysis due to these other issues.

518 Our analysis suggests that a practical limit in the benefits of increasing model accuracy may be reached when
519 resolution exceeds some threshold, as a result of other errors inherent in the modelling system. However, the
520 analysis also suggests that if these non-resolution-related errors are corrected, the benefits of adopting a smaller
521 grid cell size may be substantial. For example, meteorological data assimilation employing a dense monitoring



522 network for a specific area of interest would be expected to show a greater impact for smaller than larger grid cell
 523 sizes, due to the greater ability of the former to take advantage of the observation density in correcting the initial
 524 meteorological state. We note that recent work applying land use data assimilation (Carrera *et al.*, 2015) to
 525 regional 2.5km grid cell size weather simulations (Milbrandt *et al.*, 2016) have suggested that such data assimilation
 526 may indeed improve forecast skill at the very local scale.

527 Table 2. Surface SO₂ observations to model comparison for entire simulation period (ppbv)

Evaluation Metric	OS2.5km	OS1km	OS1km ^{A9}	OS1km ^{B9}	OS2.5km ^{B9}	OS1km ^{B49}
IoA	0.237	0.154	0.207	0.601	0.701	0.810
r	0.290	0.230	0.295	0.604	0.672	0.848
NGME	2.128	2.363	2.212	1.114	0.834	0.529
GME	2.918	3.240	3.034	1.528	1.143	0.725
CoE	-0.525	-0.693	-0.585	0.202	0.403	0.621
RMSE	7.063	9.665	7.876	4.436	3.671	2.618
NMB	1.130	1.376	1.299	0.347	-0.010	0.017
MB	1.550	1.887	1.781	0.475	-0.013	0.024

528 • 5466 Samples used

529 Table 3. Surface NO_x observations to model comparison for entire simulation period (ppbv)

Evaluation Metric	OS2.5km	OS1km	OS1km ^{A9}	OS1km ^{B9}	OS2.5km ^{B9}	OS1km ^{B49}
IoA	0.177	0.138	0.152	0.416	0.589	0.665
r	0.143	0.114	0.116	0.165	0.305	0.388
NGME	1.520	1.593	1.567	1.079	0.760	0.619
GME	12.898	13.518	13.296	9.156	6.447	5.255
CoE	-0.646	-0.725	-0.697	-0.168	0.177	0.329
RMSE	28.052	35.197	34.644	25.782	15.315	13.704



NMB	0.493	0.570	0.542	0.174	-0.027	-0.063
MB	4.183	4.834	4.597	1.477	-0.231	-0.531

530

- 3257 Samples used

531

532 Table 4. Surface O₃ observations to model comparison for entire simulation period (ppbv)

Evaluation Metric	OS2.5km	OS1km	OS1km ^{A9}	OS1km ^{B9}	OS2.5km ^{B9}	OS1km ^{B49}
IoA	0.414	0.405	0.404	0.527	0.637	0.690
r	0.496	0.506	0.515	0.606	0.688	0.738
NGME	0.660	0.670	0.672	0.534	0.410	0.349
GME	10.757	10.915	10.949	8.692	6.673	5.687
CoE	-0.172	-0.189	-0.193	0.053	0.273	0.380
RMSE	16.040	15.859	15.794	13.305	11.084	9.719
NMB	0.527	0.559	0.579	0.463	0.337	0.304
MB	8.579	9.104	9.431	7.536	5.488	4.945

533

- 2189 Samples used

534 Table 5. Surface PM_{2.5} observations to model comparison for entire simulation period (μg m⁻³)

Evaluation Metric	OS2.5km	OS1km	OS1km ^{A9}	OS1km ^{B9}	OS2.5km ^{B9}	OS1km ^{B49}
IoA	0.280	0.262	0.267	0.412	0.508	0.572
r	0.201	0.216	0.214	0.314	0.376	0.466
NGME	0.791	0.811	0.806	0.647	0.541	0.471
GME	5.342	5.478	5.441	4.365	3.651	3.181
CoE	-0.439	-0.476	-0.466	-0.176	0.016	0.143
RMSE	8.286	8.786	8.663	7.117	6.169	5.690



NMB	-0.268	-0.257	-0.257	-0.289	-0.299	-0.287
MB	-1.812	-1.734	-1.736	-1.948	-2.016	-1.937

535

- 3377 Samples used

536 The surface observation data were also analyzed by time-of-day, with both observations and simulations split into
 537 daytime (hours 9:00 to 18:00 local time) and nighttime (hour 19:00 to 8:00 local time) data pairs (Appendix, Tables
 538 A1 through A8). Within each of these diurnally segregated time periods, the broad aspects of the comparison were
 539 the same as for the “all data” Tables 2 to 5 above: the OS1km simulations tended to have reduced performance in
 540 a standard analysis, averaging improved but not completely ameliorated the performance of the OS1km simulation,
 541 a methodology employing the best of nine OS1km grid cells had superior performance to the two standard
 542 comparisons, and comparison of the “best of” methodologies for equal areas showed better performance for the
 543 OS1km compared to the OS2.5km simulation. We also noted substantial differences in the day and night
 544 performance of both models across the methodologies. For example, daytime SO₂ and NO_x performance within a
 545 given model and comparison methodology was usually better than nighttime performance for IOA,R, NGME, COE
 546 and NMB, while worse for RMSE, while nighttime O₃ performance was better for IOA, r, NGME, and COE. Daytime
 547 PM_{2.5} performance was better than nighttime for IOA, r, COE, and NMB.

548 3.2.2 Comparisons to Aircraft Observations

549 Twenty-two aircraft observation flights were carried out during the study simulation period – we present
 550 statistical comparisons using the standard approach only, here (model grid cell containing the observation point to
 551 observation data at the aircraft location). Model values were linearly interpolated in time and space to the
 552 aircraft observation locations and times (aircraft observations were on a 10s interval.) We begin with a composite
 553 comparison across all observation times, in Table 6.

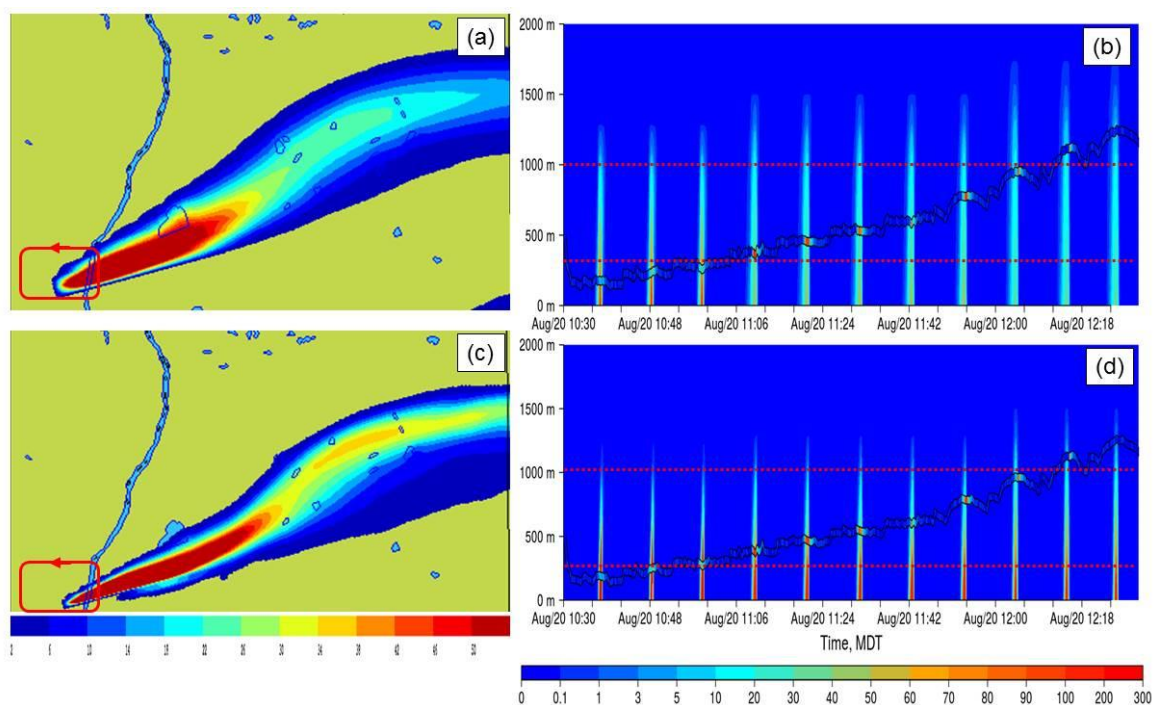
554 Table 6. Aircraft observation comparisons, SO₂ and NO₂ (ppbv)

	SO ₂ (21787 samples)		NO ₂ (18310 samples)	
	OS2.5km	OS1km	OS2.5km	OS1km
IoA	0.63	0.62	0.61	0.58
r	0.26	0.28	0.39	0.34
NGME	1.07	1.09	0.90	0.96
GME	3.98	4.06	1.56	1.68
CoE	0.27	0.25	0.23	0.17
RMSE	12.84	13.97	3.12	3.62
NMB	-0.31	-0.29	-0.26	-0.20
MB	-1.17	-1.07	-0.45	-0.34



555

556 The results are in general similar to the surface analysis, in that the OS1km simulation tended to have worse
557 performance than the OS2.5km simulation (exceptions being the biases for both SO₂ and NO₂, and the slightly
558 better OS1km correlation coefficient for SO₂). One striking difference between the first two columns of Tables 2
559 and 3 and Table 14 are the magnitude of the differences between the simulations. Aloft (Table 6), the differences
560 in performance metric magnitudes between OS2.5km and OS1km simulations are much smaller than at the
561 surface (Tables 3 and 4). The biases are negative aloft, while positive at the surface, indicating that both models
562 may be lofting plumes to insufficient distances; one of the possible (non-horizontal grid cell size dependent)
563 causes of model error may be in the extent of vertical transport (this possibility is examined in more detail in
564 Akingunola *et al.*, 2018, and Gordon *et al.*, 2018). An example of this behaviour is shown in Figure 8; both plumes
565 fumigate to the surface, while the observed plume resides largely aloft. The OS1km model captures the higher
566 concentrations to a better degree, but the impact of excessive fumigation more than offsets this improvement, as
567 is shown by the performance evaluation of Table 7, where both models have negative biases aloft. In this
568 particular case, the tendency of the model to overestimate the extent of fumigation has a bigger impact on
569 performance than grid cell size.



570

571 Figure 8. Comparison between OS2.5km (top row) and OS1km (bottom row) simulations for SO₂ relative to
572 aircraft observations (ppbv). (a,c): Simulated surface concentrations of SO₂, with the flight track shown as a red
573 line. (b,d) Simulated concentration profiles along the flight path as a function of time, with the successive



574 intersections of the flight path with the plume as background colour contours. Observed SO₂ aboard the aircraft
575 are shown between the two black lines, which show the elevation of the aircraft on successive passes around the
576 facility. Dotted lines show the upper and lower vertical extent of the observed plume. Note that for both model
577 simulations, the plume erroneously fumigates the surface.
578



579 Table 7. Standard performance evaluation of Flight 8 for SO₂ (ppbv)

	OS2.5km	OS1km
IoA	0.69	0.68
r	0.42	0.31
NGME	1.04	1.09
GME	4.02	4.25
CoE	0.39	0.35
RMSE	16.72	20.57
NMB	-0.42	-0.34
MB	-1.63	-1.32

580 1261 samples used.

581 Meanwhile other flights show a clear advantage of the OS1km model. One example is given by the NO₂
582 performance evaluation of Table 8 and depicted in Figure 9, for Flight 17 (a similar flight plan carried out around
583 the same facility as Flight 8). While the correlation coefficient degraded slightly in the OS1km resolution
584 simulation, all other performance measures were improved with the decrease in grid cell size. Two time versus
585 height profile cross-sections for Flight 17 are shown in Figure 9. In the upper two panels, the OS2.5km (Figure
586 9(a)) and OS1km (Figure 9(b)) simulations are compared for the portion of the overall flight track circling the given
587 facility. This comparison clearly shows that the OS1km model does a better job of capturing the width of the high
588 concentration region of the plume – however, the location of the model plume lags the observations. During this
589 portion of the flight alone, the OS2.5km model statistics, particularly the correlation coefficient, outperform the
590 OS1km model, due to this issue of plume location mismatching. Figures 9(a,b) may be compared to Figure 3(a,b) –
591 the same situation is depicted in both Figures. Figure 9(c,d) show the OS2.5km simulation (10(c)) and OS1km
592 simulation results in another portion of the flight – here the OS1km performance for most statistics was better
593 than the OS2.5km model performance. The OS1km model (Figure 9(d)) captures the existence of a lower
594 concentration layer aloft in the right-hand side of the cross-section, and the existence of low concentration
595 intervening layers, as well as the overall lower concentrations of SO₂, while the OS2.5km model does not resolve
596 these fine scale and lower concentration features. We note here that IoA, CoE and the other error measures
597 capture the visual impression that the OS1km model outperforms the OS2.5km model for this flight, while the
598 correlation coefficient is highly dependent on the placement of the plume maximum in the upper two panels.

599 These and the snap-shot comparisons described in Section 3.1 show that the higher resolution model is having a
600 significant impact on predictions – however, other aspects of the overall model performance are preventing the
601 potential benefits of higher resolution from influencing the standard performance evaluation.

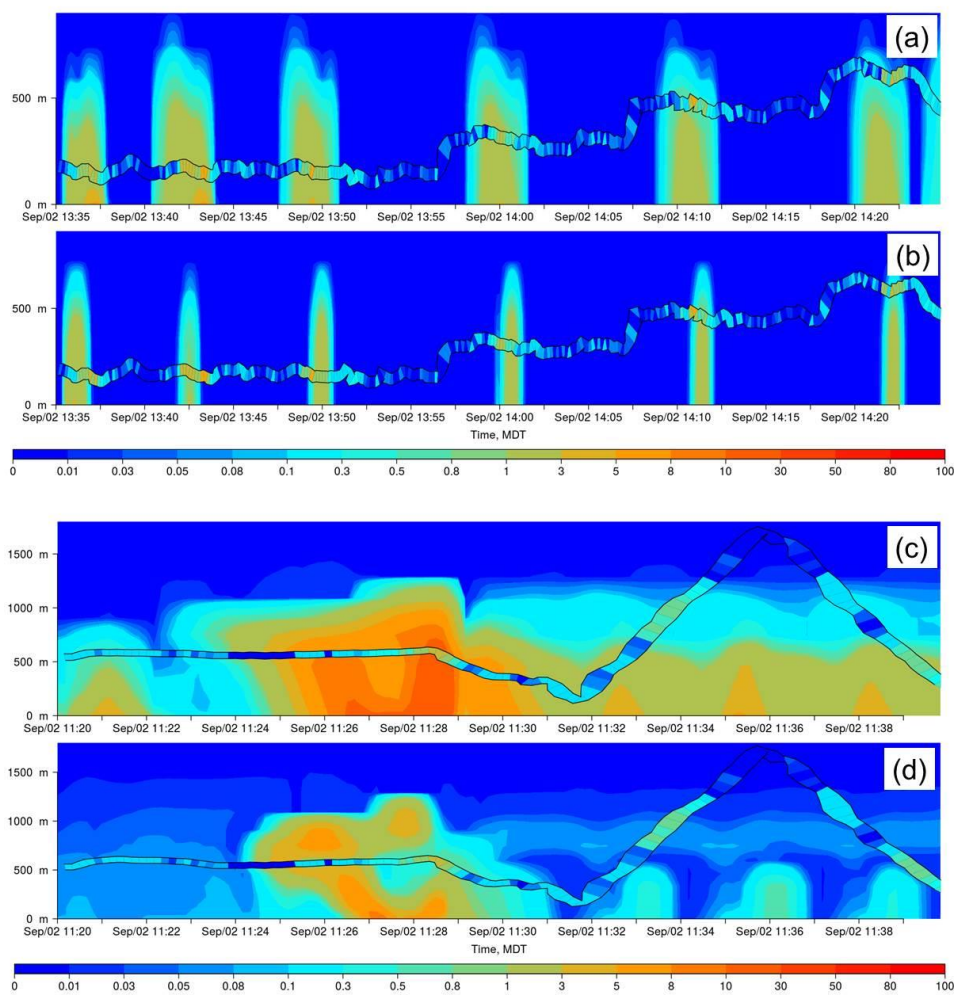
602

603



604 Table 8. Standard performance evaluation of Flight 17 for NO₂ (ppbv)

	OS2.5km	OS1km
IoA	0.26	0.58
r	0.26	0.25
NGME	2.03	1.15
GME	0.52	0.29
CoE	-0.48	0.16
RMSE	1.37	0.70
NMB	0.83	-0.54
MB	0.21	-0.14



605

606 Figure 9. Flight 17 comparison for NO₂ (ppbv) for portions of the net flight track circling the CNRL facility for
 607 OS2.5km (a) and OS1km (b) simulations, and for a later section of the same flight path for the OS2.5km (c) and
 608 OS1km (d) simulations.

609

610



611 4. Summary and Conclusions

612 Our work suggests the following:

613 Decreases to air-quality model horizontal grid cell size will not necessarily result in improvements to model
614 performance in standard performance evaluations, in which the model values at the grid-cells encompassing
615 measurement location stations are used in a pairwise comparison to observations. Other considerations, such as
616 the accuracy of the larger scale wind direction and speed forecast, and the accuracy of the plume rise
617 parameterization used within the model may play a greater role in the overall performance of the model, and
618 reduce the benefits of the smaller grid cell size. In the context of a standard model performance evaluation, there
619 may be fixed limits to the benefits of decreasing model grid cell size.

620 Despite this difficulty, our results also show that the use of smaller grid cell sizes have some potential benefits, in
621 that these models do a better job of resolving specific air pollution features, like high concentration maxima
622 within plumes. Both coarse and fine grid cell size plumes may be misplaced in both time and space, with the net
623 result that the latter model has a worse performance in a standard comparison, but is nevertheless more likely to
624 capture the correct in-plume concentrations, and hence the chemistry, of the actual plume, in the *neighbourhood*
625 of the observation location. When the evaluation is broadened to find the closest fit to observations in the vicinity
626 of the observation station, with models confined to a similar representative area around the observation station,
627 these potential benefits of the smaller grid cell size become apparent.

628 These findings suggest that at the current state of development, VHR air-quality models are of benefit for the
629 specific purpose of chemical process studies, in which the main aim of the work is to accurately simulate plume
630 chemistry – and in which accurate forecasting of the *position* of the plume in time and space is a secondary
631 concern. Our work also suggests that efforts to improve other aspects of the overall modelling framework which
632 improve the large scale flow (for example, the use of data assimilation of local meteorology to improve wind
633 direction predictions) may result in greater benefits as smaller grid cell sizes are employed.

634

635 *Acknowledgements.* The authors wish to thank the support of Environment and Climate Change Canada
636 (ECCC), under the CCAP program, for supporting this research. The authors also gratefully acknowledge the
637 assistance of Michel Valin and Sylvie Gravel for advice and assistance with the installation of GEM-MACH on the
638 Carleton University workstations during the early stages of this project.



5 References

- Akingunola, A., Makar, P.A., Zhang, J., Darlington, A., Li, S.-M., Gordon, M., Moran, M.D., Zheng, Q., A chemical transport model study of plume rise and particle size distribution for the Athabasca oil sands, *Atmos. Chem. Phys.*, 18, 8667-8688, 2018.
- Arunachalam, S., Holland, A., Do, B. & Abraczinskas, M., A quantitative assessment of the influence of grid resolution on predictions of future-year air quality in North Carolina, USA. *Atm. Env.*, 40, 5010-5026, 2006.
- Carhart, R.A., Policastro, A.J., Wastag, M., and Coke, L., Evaluation of eight short-term long-range transport models using field data, *Atm. Env.* 23, 85-105, 1989.
- Carrera, M.L., Belair, S., Bilodeau, B., The Canadian Land Data Assimilation System (CALDAS): Description and Synthetic Evaluation Study, *J. Hydromet.*, 16, 1293-1314, 2015.
- Carslaw, D. C. and Ropkins, K., openair – an R package for air quality data analysis, *Environ. Modell. Softw.*, 27–28, 52–61, 2012.
- Ching, J., Herwehe, J. and Swall, J., On joint deterministic grid modeling and sub-grid variability conceptual framework for model evaluation, *Atm. Env.*, 40, 4935-4945, 2006.
- Coiffier, J., Fundamentals of Numerical Weather Prediction, Cambridge University Press, 363pp., 2011.
- Côté, J., Gravel, S., Méthot, A., Patoine, A., Roch, M., Staniforth, A., The operational CMC--MRB global environmental multiscale (GEM) model. Part I: Design considerations and formulation, *Mon. Wea. Rev.*, 126, 1373-1395, 1998.
- Côté, J., Desmarais, J.-G., Gravel, S., Méthot, A., Patoine, A., Roch, M., Staniforth, A., The operational CMC--MRB global environmental multiscale (GEM) model. Part II: Results. *Mon. Wea. Rev.*, 126, 1397-1418, 1998.
- Dore, A. J., Kryza, M., Hall, J.R., Hallsworth, S., Keller, V.J.D., Vieno, M., and Sutton, M.A., The influence of model grid resolution on estimation of national scale nitrogen deposition and exceedance of critical loads. *Biogeosci.*, 9, 1597-1609, 2012.
- EPA, 1999: https://www.cmascenter.org/cmag/science_documentation/, last accessed September 2, 2018.
- Fox, D.G., Judging air quality model performance - summary of the AMS Workshop on Dispersion Model Performance, Woods Hole, Mass., 8-11 September 1980, *Bull. Am. Met. Soc.*, 62, 599-609, 1981.
- Fox, D.G., Uncertainty in air quality modelling – a summary of the AMS Workshop on Quantifying and Communicating Model Uncertainty, Woods Hole, Mass., September 1982, *Bull. Am. Met. Soc.*, 65, 27-36, 1984.
- Garcia-Menendez, F., Yano, A., Hu, Y. and Odman, M. T., An adaptive grid version of CMAQ for improving the resolution of plumes. *Atm. Poll. Res.*, 1, 239-249, 2010.
- Gego, E., Hogrefe, C., Kallos, G., Voudouri, A., Irwin, J.S., Rao, S.T., Examination of model predictions at different



horizontal grid resolutions. *Env. Fluid Mech.*, 5, 63-85, 2005.

Gong, W., Dastoor, A.P., Bouchet, V.S., Gong, S.L., Makar, P.A., Moran, M.D., Pabla, B., Menard, S., Crevier, L.-P., Cousineau, S., Venkatesh, S., Cloud processing of gases and aerosols in a regional air quality model (AURAMS), *Atm. Res.* 82, 248-275, 2006.

Gong, W., Makar, P.A., Zhang, J., Milbrandt, M., Gravel, S., Hayden, K.L., MacDonald, A.M., Leitch, W.R., Modelling aerosol–cloud–meteorology interaction: A case study with a fully coupled air quality model (GEM-MACH). *Atm. Env.*, 115, 695-715, 2015.

Gong, S.L., Barrie, L.A., Lazare, M., Canadian Aerosol Module (CAM): a size-segregated simulation of atmospheric aerosol processes for climate and air quality models: 2. Global sea-salt aerosol and its budgets. *J. Geophys. Res.* 107, 4779. <http://dx.doi.org/10.1029/2001JD002004>, 2003a.

Gong, S. L., Barrie, L.A., Blanchet, J.-P., von Salzen, K., Lohmann, U., Lesins, G., Spacek, L., Zhang, L.M., Girard, E., Lin, H., Leitch, R., Leighton, H., Chylek, P., Huang, P., Canadian Aerosol Module: A size-segregated simulation of atmospheric aerosol processes for climate and air quality models 1. Module development. *J. Geophys. Res.*, 108, D1, 4007, doi:10.1029/2001JD002002, 2003b.

Gordon, M., Makar, P.A., Staebler, R., Zhang, J., Akingunola, A., Gong, W., Li, S.-M., A comparison of plume rise algorithms to stack plume measurements in the Athabasca oil sands, *Atm. Chem. Phys. Disc.*, (<https://www.atmos-chem-phys-discuss.net/acp-2017-1093/>), 2018.

Government of Alberta, 2016: Alberta Energy: Oil Sands, <http://www.energy.alberta.ca/oilsands/oilsands.asp>, 2016, last accessed November 11, 2017.

Grasso, L.D., The differentiation between grid spacing and resolution and their application to numerical modelling, *Bull. Am. Met. Soc.*, 81, 579-580, 2000.

Hanha, S.R., Air quality model evaluation and uncertainty. *J. Air Poll. Cont. Assoc.*, 33, 406-412, 1988.

Isakov, V., Irwin, J. S., Ching, J., Using CMAQ for exposure modeling and characterizing the subgrid variability for exposure estimates. *J. App. Met. Clim.*, 46, 1354-1371, 2007.

Jacobson, M.Z., Fundamentals of Atmospheric Modelling, Cambridge U. Press, 656pp., 1999.

Kang, D., Mathur, R., Schere, K., Yu, S., Eder, B., New categorical metrics for air quality model evaluation, *J. App. Met. Clim.*, 46, 549-555, 2007.

Kumar, N., Russell, A.G., Segall, E., Steenkiste, P. Parallel and Distributed Application of an Urban-to-Regional Multiscale Model. *Comp. Chem. Eng.*, 21, 399-408, 1997.

Lee, I.Y., Numerical simulations of cross-Appalachian transport and diffusion. *Bound. Lay. Met.*, 39, 53-66, 1987.

Lonsdale, C.R., Stevens, R.G., Brock, C.A., Makar, P.A., Knipping, E.M., and Pierce J.R., The effect of coal-fired power-plant SO₂ and NO_x control technologies on aerosol nucleation in the source plumes, *Atm. Chem. Phys.*, 12, 11519-11531, 2012.



- Makar, P. A., Bouchet, V. S. & Nenes, A., Inorganic chemistry calculations using HETV—a vectorized solver for the SO₄--NO₃--NH₄⁺ system based on the ISORROPIA algorithms. *Atm. Env.*, 37, 2279-2294, 2003.
- Makar, P.A., Gong, W., Milbrandt, J., Hogrefe, C., Zhang, Y., Curci, G., Zabkar, R., Im, U., Balzarini, A., Baro, R., Bianconi, R., Cheung, P., Forkel, R., Gravel, S., Hirtl, H., Honzak, L., Hou, A., Jimenz-Guerrero, P., Langer, M., Moran, M.D., Pabla, B., Perez, J.L., Pirovano, G., San Jose, R., Tuccella, P., Werhahn, J., Zhang, J., Galmarini, S., Feedbacks between air pollution and weather, part 1: Effects on weather. *Atm. Env.*, 115, 442-469, 2015(a).
- Makar, P.A., Gong, W., Hogrefe, C., Zhang, Y., Curci, G., Zabkar, R., Milbrandt, J., Im, U., Balzarini, A., Baro, R., Bianconi, R., Cheung, P., Forkel, R., Gravel, S., Hirtl, H., Honzak, L., Hou, A., Jimenz-Guerrero, P., Langer, M., Moran, M.D., Pabla, B., Perez, J.L., Pirovano, G., San Jose, R., Tuccella, P., Werhahn, J., Zhang, J., Galmarini, S., Feedbacks between air pollution and weather, part 2: Effects on chemistry. *Atm. Env.*, 115, 499-526, 2015(b).
- Markakis, K., Valari, M., Perrussel, O., Sanchez, O., and Honore, C., Climate-forced air-quality modeling at the urban scale : sensitivity to model resolution, emissions and meteorology. *Atm. Chem. Phys.*, 15, 7703-7723, 2015.
- Milbrandt, J. A. and Yau, M. K., A multimoment bulk microphysics parameterization, Part I: analysis of the role of the spectral shape parameter, *J. Atmos. Sci.*, 62, 3051–3064, 2005(a).
- Milbrandt, J. A. and Yau, M. K., A multimoment bulk microphysics parameterization, Part II: a proposed three-moment closure and scheme, *J. Atmos. Sci.*, 62, 3065–3081, 2005(b).
- Milbrandt, J.A., Belair, S., Faucher, M., Vallee, M., Carrera, M.L., and Glazer, A., The Pan-Canadian high resolution deterministic prediction system, *Weather and Forecasting*, 31, 1791-1816, 2016.
- Moran, M. D. Ménard, S., Talbot, D., Huang, P., Makar, P. A., Gong, W., Landry, H., Gravel, S., Gong, S., Crevier, L.-P., Kallaur, A., Sassi, M., Particulate-matter forecasting with GEM-MACH15, a new Canadian air-quality forecast model. *Air pollution modelling and its application XX*. Springer, Dordrecht, pp. 289-292, 2010.
- Pepe, N., Pirovano, G., Lonati, G., Balzarini, A., Toppetti, A., Riva, G.M., and Bedogni, M., Development and application of a high resolution hybrid modelling system for the evaluation of urban air quality. *Atm. Env.*, 141, 297-311, 2016.
- Pielke, R.A. Sr., Further comments on "The differentiation between grid spacing and resolution and their application to numerical modeling", *Bull. Am. Met. Soc.*, 82, 699, 2001.
- Queen, A. and Zhang, Y., Examining the sensitivity of MM5--CMAQ predictions to explicit microphysics schemes and horizontal grid resolutions, Part III—The impact of horizontal grid resolution. *Atm. Env.*, 42, 3869-3881, 2008.
- Salvador, R., Calbó, J. & Millán, M. M., Horizontal grid size selection and its influence on mesoscale model simulations. *J. App. Met.*, 38, 1311-1329, 1999.



- Shrestha, K. L., Kondo, A., Akikazu, K. A. G. A., Inoue, Y., High-resolution modeling and evaluation of ozone air quality of Osaka using MM5-CMAQ system. *J. Env. Sci.*, 21, 782-789, 2009.
- Sillman, S., Vautard, R., Menut, L. & Kley, D., O₃-NO_x-VOC sensitivity and NO_x-VOC indicators in Paris: Results from models and Atmospheric Pollution Over the Paris Area (ESQUIF) measurements. *J. of Geophys. Res.*, 108, 8563, doi:10.1029/2002JD001561, 2003.
- Stroud, C.A., P.A. Makar, M.D. Moran, W. Gong, S. Gong, J. Zhang, K. Hayden, C. Mihele, and J.R. Brook, Impact of model grid spacing on regional- and urban-scale air quality predictions of organic aerosol. *Atm. Chem. Phys.*, 11, 3,107-3,118, 2011.
- Valari, M. and Menut, L., Does an increase in air quality models' resolution bring surface ozone concentrations closer to reality?. *J. Atm. Ocean. Tech.*, 25, 1955-1968, 2008.
- Vardoulakis, S., Fisher, B. E. A., Pericleous, K., Gonzalez-Flesca, N., Modelling air quality in street canyons: a review. *Atm. Env.*, 37, 155-182, 2003.
- Wolke, R., Schröder, W., Schrödner, R., Renner, E., Influence of grid resolution and meteorological forcing on simulated European air quality: a sensitivity study with the modeling system COSMO--MUSCAT. *Atm. Env.*, 53, 110-130, 2012.
- Zhang, J, Moran, M.D., Zheng, Q., Makar, P.A., Baratzadeh, P., Marson, G., Liu, P., Li, S.-M., Emissions preparation and analysis for multiscale air quality modeling over the Athabasca Oil Sands Region of Alberta, Canada, *Atm. Chem. Phys.*, 18, 10459–10481, 2018.



6. Appendix A: Model Evaluation Statistics

Table A1. Model comparison statistics

Metric and Formula	Range	Ideal Score
$IOA = \begin{cases} 1 - \frac{\sum M_i - O_i }{2(O_i - \bar{O})}, & \text{when } \sum M_i - O_i \leq 2(O_i - \bar{O}) \\ \frac{2(O_i - \bar{O})}{\sum M_i - O_i } - 1, & \text{when } \sum M_i - O_i > 2(O_i - \bar{O}) \end{cases}$	[-1,1]	1
$CoE = 1 - \frac{\sum M_i - O_i }{(O_i - \bar{O})}$	$[-\infty, 1]$	1
$MB = \frac{1}{N} \sum (M_i - O_i) = \bar{M} - \bar{O}$		0
$MGE = \frac{1}{N} \sum M_i - O_i $		0
$NMB = \frac{\sum (M_i - O_i)}{\sum O_i} = \left(\frac{\bar{M}}{\bar{O}} - 1 \right)$		0
$NMGE = \frac{\sum M_i - O_i }{\sum O_i}$		
$RMSE = \sqrt{\frac{1}{N} \sum (M_i - O_i)^2}$		
$r = \frac{\sum (M_i - \bar{M})(O_i - \bar{O})}{\sqrt{\sum (M_i - \bar{M})^2 \sum (O_i - \bar{O})^2}}$	[-1.1]	1

The limits on the summations were removed for brevity; all are from $i = 1$ to N where N is the number of observation-model pairs, M_i is the i 'th model value, O is the i 'th observation value, and \bar{M}, \bar{O} are the model and observed mean values, respectively.



7. Appendix B: Day Versus Night model performance for the different testing methodologies

Table B1. Surface SO₂ observations to model comparison, daytime (9:00-18:00) (ppbv).

	OS2.5km	OS1km	OS1km ^{A9}	OS1km ^{B9}	OS2.5km ^{B9}	OS1km ^{B49}
IoA	0.374	0.286	0.352	0.712	0.762	0.872
r	0.295	0.215	0.307	0.701	0.742	0.903
NGME	1.739	1.982	1.798	0.799	0.660	0.356
GME	4.201	4.788	4.343	1.931	1.595	0.860
CoE	-0.253	-0.428	-0.295	0.424	0.524	0.744
RMSE	9.317	13.388	10.275	5.171	4.652	2.996
NMB	0.730	0.990	0.871	0.054	-0.166	-0.118
MB	1.764	2.391	2.104	0.132	-0.401	-0.286

- 2119 Samples used

Table B2. Surface SO₂ observations to model comparison, nighttime (18:00-9:00) (ppbv).

	OS2.5km	OS1km	OS1km ^{A9}	OS1km ^{B9}	OS2.5km ^{B9}	OS1km ^{B49}
IoA	-0.215	-0.248	-0.233	0.231	0.473	0.609
r	0.204	0.206	0.205	0.339	0.421	0.620
NGME	3.143	3.281	3.215	1.896	1.300	0.964
GME	2.061	2.152	2.108	1.243	0.852	0.632
CoE	-1.549	-1.607	-1.607	-0.537	-0.054	0.218
RMSE	5.055	5.450	5.450	3.802	2.858	2.313
NMB	2.166	2.328	2.328	1.076	0.394	0.361
MB	1.421	1.527	1.527	0.706	0.258	0.230

- 3347 Samples used

Table B3. Surface NO_x observations to model comparison, daytime (9:00-18:00) (ppbv).

	OS2.5km	OS1km	OS1km ^{A9}	OS1km ^{B9}	OS2.5km ^{B9}	OS1km ^{B49}
IoA	0.485	0.440	0.465	0.639	0.712	0.789
r	0.254	0.259	0.270	0.427	0.507	0.680
NGME	0.927	1.009	0.962	0.650	0.519	0.380
GME	7.502	8.160	7.786	5.259	4.198	3.077
CoE	-0.030	-0.120	-0.069	0.278	0.424	0.577
RMSE	14.843	15.811	15.571	11.272	9.982	7.964
NMB	-0.205	-0.069	-0.135	-0.258	-0.258	-0.216
MB	-1.659	-0.559	-1.091	-2.089	-2.091	-1.744

- 1252 Samples used

Table B4. Surface NO_x observations to model comparison, nighttime (18:00-9:00) (ppbv).

	OS2.5km	OS1km	OS1km ^{A9}	OS1km ^{B9}	OS2.5km ^{B9}	OS1km ^{B49}
IoA	-0.016	-0.050	-0.045	0.275	0.511	0.587
R	0.113	0.081	0.083	0.118	0.240	0.295
NGME	1.913	1.982	1.971	1.366	0.920	0.777
GME	17.235	17.858	17.756	12.306	8.291	7.004
CoE	-1.032	-1.105	-1.093	-0.451	0.023	0.174
RMSE	35.003	44.669	43.972	32.797	18.475	16.875
NMB	0.958	0.988	0.990	0.458	0.126	0.039
MB	8.634	8.899	8.915	4.124	1.139	0.350

- 1862 Samples used

Table B5. Surface O₃ observations to model comparison, daytime (9:00-18:00) (ppbv).

	OS2.5km	OS1km	OS1km ^{A9}	OS1km ^{B9}	OS2.5km ^{B9}	OS1km ^{B49}
IoA	0.141	0.192	0.184	0.338	0.396	0.529
r	0.166	0.215	0.211	0.327	0.367	0.504
NGME	0.660	0.621	0.627	0.508	0.464	0.361
GME	14.427	13.568	13.703	11.111	10.143	7.901
CoE	-0.718	-0.616	-0.632	-0.323	-0.208	0.059
RMSE	21.209	20.063	20.035	16.714	15.140	12.466
NMB	0.587	0.542	0.557	0.454	0.414	0.326
MB	12.839	11.854	12.187	9.918	9.050	7.121

- 864 Samples used

Table B6. Surface O₃ observations to model comparison, nighttime (18:00 to 9:00) (ppbv).

	OS2.5km	OS1km	OS1km ^{A9}	OS1km ^{B9}	OS2.5km ^{B9}	OS1km ^{B49}
IoA	0.451	0.398	0.399	0.534	0.719	0.727
r	0.526	0.541	0.557	0.642	0.784	0.784
NGME	0.706	0.775	0.773	0.600	0.361	0.352
GME	8.326	9.132	9.116	7.070	4.258	4.145
CoE	-0.097	-0.203	-0.201	0.068	0.439	0.454
RMSE	11.236	12.029	11.974	10.297	6.935	7.137
NMB	0.492	0.624	0.651	0.510	0.262	0.296
MB	5.799	7.359	7.668	6.008	3.088	3.491

- 1247 Samples used

Table B7. Surface PM_{2.5} observations to model comparison, daytime (9:00-18:00) ($\mu\text{g m}^{-3}$).

	OS2.5km	OS1km	OS1km ^{A9}	OS1km ^{B9}	OS2.5km ^{B9}	OS1km ^{B49}
IoA	0.372	0.356	0.364	0.495	0.555	0.625
r	0.232	0.244	0.245	0.350	0.387	0.493
NGME	0.816	0.837	0.827	0.657	0.579	0.487
GME	5.470	5.608	5.542	4.402	3.879	3.266
CoE	-0.256	-0.288	-0.272	-0.011	0.109	0.250
RMSE	9.607	10.312	10.034	8.059	7.286	6.626
NMB	-0.189	-0.152	-0.166	-0.231	-0.281	-0.258
MB	-1.264	-1.016	-1.109	-1.546	-1.881	-1.726

- 1862 Samples used

Table B8. Surface PM_{2.5} observations to model comparison, nighttime (18:00 to 9:00) ($\mu\text{g m}^{-3}$)

	OS2.5km	OS1km	OS1km ^{A9}	OS1km ^{B9}	OS2.5km ^{B9}	OS1km ^{B49}
IoA	0.193	0.170	0.173	0.337	0.471	0.528
r	0.163	0.183	0.178	0.277	0.368	0.442
NGME	0.782	0.804	0.801	0.642	0.512	0.457
GME	5.313	5.466	5.444	4.367	3.483	3.105
CoE	-0.614	-0.660	-0.653	-0.326	-0.058	0.057
RMSE	7.467	7.841	7.834	6.542	5.373	5.032
NMB	-0.293	-0.302	-0.293	-0.309	-0.293	-0.294
MB	-1.992	-2.050	-1.989	-2.098	-1.991	-1.995

- Samples used